UNIVERSITY OF COPENHAGEN
NIELS BOHR INSTITUTE

New Limits on the Neutrino Lifetime Using the Flavour Composition of High-Energy Astrophysical Neutrinos

Bachelor Thesis

Supervised by Mauricio Bustamante and Poul Henrik Damgaard, NBI

Jonathan Baltazar Steensgaard

Submission date: 16/06-2021

Jonathan Baltazar — *Signature*

16/6-2021 — *Date*

Acknowledgements

I want to express my sincerest gratitude to my supervisor Mauricio Bustamante, for his exceptional guidance, advice and engagement throughout the entire project. Thank you for turning my interest to the amazing world of neutrino physics. A special thank you to my father Ole and my friend Amalie for their attention to detail and their helpful comments.

Abstract

In the field of neutrino physics there are several indications of phenomena beyond the Standard Model such as neutrino decay. If the heavier neutrinos decay into the lighter ones, neutrino decay could uniquely influence the relative flavor composition of the flux of high-energy neutrinos, especially if the coupling (g_{ij}) between the decaying neutrino and the daughter particle is large. Because high-energy astrophysical neutrinos (TeV–PeV energies) travel cosmological distances, they are an excellent source for examining decay. Using recent measurements of the flavor composition from IceCube, we place new limits on the coupling between the neutrino states. To do so, we employ a model of visible neutrino decay where the daughter particles contribute to the detected neutrino flux. With this we carry out a large parameter scan and compute a substantial data set of the theoretical flavor compositions at Earth with decay. With a Bayesian approach, including the likelihood functions from IceCube, we find the upper limit of the couplings as: $\log g_{21} < -0.27$, $\log g_{31} < -7.06$, and $\log g_{32} < -7.05$. Based on the estimated flavor sensitivity of current and upcoming neutrino telescopes, we forecast the constraints of neutrino decay that they will be able to place. We placed a new lower limit of the lifetime of the neutrino mass eigenstate ν_3 which is considerably better than previous ones, while the lower limit found on the lifetime on ν_2 is significantly weaker.

The source code for the visible decay model from Ref. [1], used in the project can be found at `https://github.com/PeterDenton/Astro-Nu-Decay`. The extended code for this specific project is provided at `https://github.com/JonnaBaltazar/Bachelor-Project`.

Contents

1 Introduction

Neutrinos are among the most abundant elementary particles in the Universe, but several of their properties are still unknown. In the Standard Model, neutrinos were constructed as massless and stable. However, later experiments have revealed that they undergo flavor oscillations, and a striking consequence of this behavior is that neutrinos have mass. Today, we know that each of the three neutrino flavors ($\nu_e, \nu_m u, \nu_t au$) is a superposition of three mass eigenstates (ν_1, ν_2, ν_3) [2] [3].
Neutrino decay is a proposed mechanism in which the heaviest neutrino states may decay into the lightest ones or new particles entirely. Within the Standard Model, neutrinos can decay, but the associated lifetime is at least 10^{43}s, which is orders of magnitude longer than the age of the Universe [4][5][6]. However, several theories postulate the decay of neutrinos into new particles. If the coupling between neutrinos and the daughter particle is strong, neutrino decay could occur at a higher rate than in the Standard Model. The decay would modify the flavor composition — i.e., the relative abundance of neutrinos of each flavor — of neutrinos observed at Earth and possibly yield detectable evidence [3].
Several experiments have searched for the effects of neutrino decay, using primarily reactor, solar, and atmospheric neutrinos. The impact of the decay is so minuscule that the neutrinos require a long baseline, such that the effects accumulate along the way to have a noticeable influence on the final composition. Thereby, high-energy astrophysical neutrinos, with sources possibly located outside our galaxy traveling cosmological-scale distances, are great candidates to probe these tiny effects. The IceCube Neutrino Observatory regularly detects these high-energy astrophysical neutrinos (in the TeV - PeV range) and has recently identified events stemming from ν_τ [7]. The measurement of the flavor composition can be utilized to study physics outside of the Standard Model, and if IceCube does not find evidence of decay, the composition can be exploited to constrain the neutrino lifetime [8] [9] [10].

This project aims at improving our understanding of the properties of neutrino decay and to constrain the lifetimes of the neutrino mass eigenstates. We adopt the general decay framework from Ref. [1], where the daughter neutrinos in the decay are visible, i.e., they contribute to the detected neutrino flux. This is a model-independent approach where the identity of the new particle is unspecified, other than being a massive scalar (i.e., spin-0) boson.
We utilize the visible-decay model to compute the final flavor compositions at Earth and analyze the effect of varying the decay parameters. Afterward, we perform a large parameter scan to obtain a substantial data set of theoretical final flavor composition. This is superimposed with the likelihood functions of flavor composition from IceCube [11], where the parameters of the decay are kept free. Through a Bayesian approach, we provide a new upper limit on the lifetimes of neutrinos.

Throughout, we assume normal neutrino mass ordering (i.e., $m_{\nu_1} < m_{\nu_2} < m_{\nu_3}$); an extension to inverted ordering is possible, but beyond the scope of this work. Besides we use natural units; $\hbar = c = 1$.

2 Theory and experimental background

In this section, we present the relevant theoretical background necessary for understanding the decay framework. Furthermore, we include a description of the IceCube Neutrino Observatory along with how this determines the flavor of the observed neutrinos.

2.1 Standard Model

The Standard Model describes elementary particles and the interactions between them. The matter particles are fermions with half-odd integer spins, and the interacting particles are bosons with integer spins. The model splits the fermions into two different groups: *quarks* and *leptons*.
Quarks make up hadrons, subatomic composite particles comprised of either two or three quarks, called mesons and baryons. The quarks are categorized into three families of increasing mass, where the lightest family, up and down quarks, build up protons and neutrons. The leptons are also classified into families: charged leptons (e, μ, τ) and corresponding neutral leptons, or neutrinos $(\nu_e, \nu_\mu, \nu_\tau)$ [2].
There are four fundamental interactions; gravity, electromagnetism, the strong-, and the weak interaction. The interactions are mediated by bosons which are, respectively, the graviton (proposed, but not yet detected), the photon, the gluon, and the W- and Z-bosons.

2.2 Neutrino Mixing and Oscillations

The discovery that neutrinos can change flavor — known as *neutrino oscillation* — was a significant breakthrough in particle physics. As a result of the oscillations, there is an intrinsic probability that a neutrino created in a specific flavor state is detected in a different state after propagating away from its source [12].
Oscillations are resolved by introducing neutrino mass eigenstates, ν_i with $i = 1, 2, 3$, each with a definite mass m_i. The neutrino flavor state is defined as a superposition of the mass eigenstates [12], and so does not have a well-defined mass. The masses m_i are presently unknown, but in this thesis we assume the normal mass ordering $(m_1 < m_2 < m_3)$ [13] to be correct.
The coefficients $U_{\alpha i}$ that appear in the superposition of mass eigenstates are organized in the *Pontecorvo–Maki–Nakagawa–Sakata* (PMNS) matrix [2]

$$\begin{pmatrix} \nu_e \\ \nu_\mu \\ \nu_\tau \end{pmatrix} = \begin{pmatrix} U_{e1} & U_{e2} & U_{e3} \\ U_{\mu 1} & U_{\mu 2} & U_{\mu 3} \\ U_{\tau 1} & U_{\tau 2} & U_{\tau 3} \end{pmatrix} \begin{pmatrix} \nu_1 \\ \nu_2 \\ \nu_3 \end{pmatrix}, \tag{1}$$

known as the lepton mixing matrix. Following the convention in Ref. [14] it can be parametrized in terms of the mixing parameters; three angles $(\theta_{12}, \theta_{13}, \theta_{23})$ and a CP-violating phase (δ_{CP}). Thus the

PMNS matrix can be written as a product of three rotation matrices, i.e.,

$$U = \begin{pmatrix} 1 & 0 & 0 \\ 0 & c_{23} & s_{23} \\ 0 & -s_{23} & c_{23} \end{pmatrix} \begin{pmatrix} c_{13} & 0 & s_{13}e^{-i\delta_{CP}} \\ 0 & 1 & 0 \\ -s_{13}e^{i\delta_{CP}} & 0 & c_{13} \end{pmatrix} \begin{pmatrix} c_{12} & s_{12} & 0 \\ -s_{12} & c_{12} & 0 \\ 0 & 0 & 1 \end{pmatrix} \tag{2}$$

where $s_{ij} \equiv \sin\theta_{ij}$, $c_{ij} \equiv \cos\theta_{ij}$.
The flavor-transition probability of a ν_α of energy E changing into a ν_β after traveling a distance L from its source is [12]

$$P_{\alpha\longrightarrow\beta} = \delta_{\alpha\beta} - 4\sum_{i>j} \mathrm{Re}\left(U^*_{\alpha i}U_{\beta i}U_{\alpha j}U^*_{\beta j}\right)\sin^2\left(\Delta m^2_{ij}\frac{L}{4E}\right) + 2\sum_{i>j}\mathrm{Im}\left(U^*_{\alpha i}U_{\beta i}U_{\alpha j}U^*_{\beta j}\right)\sin\left(\Delta m^2_{ij}\frac{L}{2E}\right). \tag{3}$$

where $\Delta m^2_{21} = 7.42\cdot 10^{-5}\mathrm{eV}^2$ and $\Delta m^2_{31} = 2.541\cdot 10^{-3}\mathrm{eV}^2$ are values from ν-fit 5.
Because neutrinos are typically ultra-relativistic, we can approximate the propagation time $t \sim L$. For neutrinos at 1 TeV, the oscillation length is around 0.1pc [15]. Since the astrophysical neutrinos have baselines on cosmological distances ($\sim$ Gpc), the oscillations are too fast to resolve. Therefore, the transition probability is averaged out and can be simplified to

$$P_{\alpha\to\beta} = \sum_{i=1}^{3} |U_{\alpha i}|^2 |U_{\beta i}|^2 \,. \tag{4}$$

2.3 High-Energy Astrophysical Neutrinos

High-energy neutrinos of astrophysical origin have been hypothesized for many years and were finally discovered by IceCube in 2013 [16]. These neutrinos are created in astrophysical sources primarily through the decay of charged pions created in cosmic-ray interactions with radiation or gas. The complete interaction chain is

$$p + \gamma \text{ (or } p + p) \longrightarrow \Delta^+ \longrightarrow \pi^+ \longrightarrow \mu + \bar{\nu_\mu} \longrightarrow e^+ + \nu_e + \nu_\mu + \bar{\nu_\mu}\,. \tag{5}$$

They are likely produced in extragalactic cosmic-particle accelerators, and when resulting from pion decay, the neutrinos accrue about 5% of the cosmic ray energy [16]. Figure 1 shows the Feynman diagram for pion decay.
This type of decay results in an initial flavor composition of $(f_{e,\mathrm{S}} : f_{\mu,\mathrm{S}} : f_{\tau,\mathrm{S}}) = (1 : 2 : 0)$ at the source. The flavor composition is a measure of the ratio of neutrinos, adding neutrinos and anti-neutrinos since large-scale neutrino telescopes like IceCube cannot easily distinguish between them experimentally. When computing the compositions, we define the flavor ratios f_α that are normalized

with the constraint $f_e + f_\mu + f_\tau = 1$.

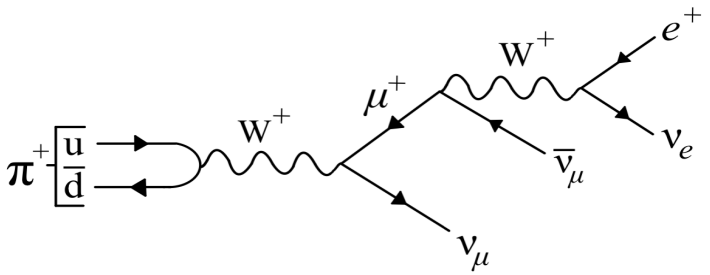

Figure 1. Feynman diagram of a pion decay resulting in high-energy astrophysical neutrinos.

2.4 IceCube Neutrino Observatory

The flavor ratios we compute in this project are processed with likelihood functions of flavor compositions from the IceCube Neutrino Observatory. IceCube is the largest neutrino telescope to date, at a cubic-kilometer scale, and is located at the South Pole. It consists of an array of subsurface digital optical modules (DOMs), each with a photo-multiplier tube [17]. Since neutrinos have a small interaction cross section, detecting them requires a substantial detector volume. The icecap at the South Pole provides a convenient detection site, as it offers a vast quantity of interaction material along with a transparent medium wherein light from neutrino-initiated particle showers can propagate over significant distances [15].

Neutrinos only interact via the weak interaction, which can be mediated by either the $W^\pm$-boson, charged-current interactions (CC), or the Z^0-boson, neutral-current interactions (NC). In IceCube, neutrinos interact with the surrounding ice striking either a proton or a neutron, and for CC interactions, exchanging a W boson and transforming into a charged lepton. The charged lepton is always of the same flavor as the neutrino [12].

As the charged leptons pass through a medium with a non-zero refractive index, such as ice, they may travel faster than the phase velocity of light. Consequently, the particles emit Cerenkov photons, which IceCube uses to retrace the collision point and identify the neutrino flavor, energy, and incoming direction [17].

2.5 Determining Flavor at IceCube

In IceCube, high-energy neutrinos deep-inelastic-scatter on the nucleons in the ice. The neutrino can shred apart the quark bonds at these energies, enabling the formation of new particles [15]. The flavor of an interacting neutrino can be inferred through the distinct Cherenkov light pattern produced by the charged secondary particles resulting from a neutrino interaction. As mentioned earlier, neutrinos can

interact through both CC and NC interactions which have distinct signatures.
Events in IceCube are categorized into three different topologies: **tracks, single cascades**, and **double cascades**. All the events are reconstructed with maximum likelihood fits of the different hypotheses, and the event is classified through the best fit [7]. These event types can be seen in Fig. 2.

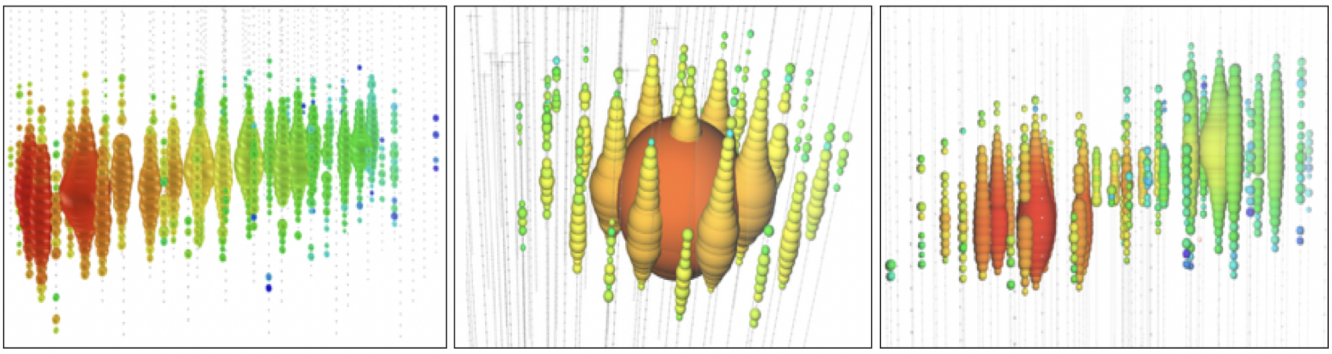

Figure 2. Examples of the three different types of events observed at IceCube, from left to right; *track, single cascade,* and *double cascade.* This is a simulated double cascade. Each sphere represents a DOM recording the Cherenkov light, while the color indicates the amount of observed light. Figure from Ref. [11].

The *track* events are created by the light deposits from a muon traversing the detector, resulting from either a ν_μ CC interaction or a ν_τ CC interaction where the tauon decays to a muon (17% branching ratio). These are easily distinguishable from a single or double cascade. The *single cascade* events are energy deposits at a single vertex and originate from either NC interactions of any flavor or the CC interactions of ν_e and ν_τ. With the single cascades, it is impossible to distinguish ν_e from ν_τ on an event-by-event basis. A *double cascade* is two energy deposits connected by a track, which can only occur by a ν_τ CC interaction. Here the first cascade originates from a hadronic interaction wherein a tauon is produced. This tauon traverses the detector, leaving a track, before decaying due to the short lifetime and creating either a hadronic or electromagnetic cascade (83% branching ratio) [7].

2.6 New ν_τ Results

The motivation behind this project was utilizing the new data published by IceCube; the first-ever clearly identified ν_τ events with the double cascade topology [7]. IceCube has incorporated these data into their projected likelihood functions for the flavor composition of high-energy astrophysical neutrinos [11]. To constrain the lifetime of neutrinos, we will employ several estimated likelihood functions: the current 8yr likelihood function, the expected likelihood after 15 years, the expected likelihood after 15yr as well as introducing Generation 2 for 10yr, and finally, the combined likelihood from future neutrino experiments combined. They were obtained from Ref. [11][18].

3 Decay Framework

In this section, we will follow the decay formalism presented in Ref.[1], with the corresponding code, which we have adapted to our case. Initially, we present the different characters of the decay, along with the expressions that govern these. Afterwards, we incorporate cosmology to correct these expressions for the effects of the expanding Universe.

The astrophysical neutrinos emerge at initial energy and flux (E_i, Φ_α^S) from the source, then propagate on a baseline L, to later be observed at the Earth with energy and flux (E_f,$\Phi_{\alpha\beta}^E$). If neutrinos are decaying along the baseline, the final flux ν_β would be smaller than the standard expectation based on oscillation. The probability of transition is defined as the observed neutrino spectrum over the initial spectrum at the source [1], i.e.,

$$P_{\alpha\beta} = \frac{\Phi_{\alpha\beta}^E(E_f)}{\Phi_\alpha^S(E_i)}. \tag{6}$$

In agreement with IceCube observations, we take the initial neutrino spectrum to be a power law

$$\Phi_\alpha^S = \Phi_0^S E_f^{-\gamma}\,, \tag{7}$$

where γ is the spectral index. In our analysis, we vary the value of γ.
A mechanism that generates neutrino decay postulates a Goldstone boson called the Majoron, ϕ, created through the spontaneous breaking of the global lepton-number symmetry [3]. Such a model would induce a decay of the heavier mass eigenstates into the lighter ones, $\nu_i \to \nu_j + \phi$. In this project, neutrinos will be assumed to be Majorana, i.e., $\nu = \overline{\nu}$. The Lagrangian that describes decay is [1]

$$L \supset \frac{g_{ij}}{2}\overline{\nu_j}\nu_i\phi + \frac{g'_{ij}}{2}\overline{\nu_j}i\gamma_5\nu_i\phi + \text{h.c.} \tag{8}$$

where the scalar and pseudo-scalar couplings are given by g_{ij} and g'_{ij}, respectively. The coupling constants and the lifetime are associated via the relationship $\tau_i = m_i/E_i\Gamma_i$, where the decay width Γ_i (Appendix A) is a function of the couplings. Thus constraining the coupling leads to a constraint on the lifetime.

3.1 Visible and Invisible Decay

We consider three distinct decay modes between mass states: $\nu_3 \to \nu_1$, $\nu_2 \to \nu_1$, and the intermediate decay $\nu_3 \to \nu_2 \to \nu_1$. The corresponding couplings are; g_{21}, g_{31} and g_{32}, with $g_{ij} = g'_{ij}$.
Two distinctive decays can be identified; **visible** and **invisible decay**. [13]
For invisible decay, the final neutrino state is undetectable, which is either because the state is sterile

or that the state has an energy that lies outside the observable range. This is expressed by a depletion term, $\bar{P}^{\rm dep}_{\alpha_\beta}(E_f)$, leading to the observation of fewer ν_μ and ν_τ.
For visible decay, the final state neutrino is observable and contributes to the flux, though with a lower energy than the parent neutrino, leading to a depletion of the heavier states and an accompanying increase in the lightest states, expressed by the regeneration term $\bar{P}^{\rm reg}_{\alpha_\beta}(E_f)$. Lastly, there is a standard transition probability (i.e., no decay), $\bar{P}^{\rm SM}_{\alpha\beta}$. Putting all these terms together gives us the complete transition probability of visible decay [1],

$$\bar{P}^{\rm vis}_{\alpha\beta}(E_f) = \bar{P}^{\rm SM}_{\alpha\beta} + \bar{P}^{\rm dep}_{\alpha\beta}(E_f) + \bar{P}^{\rm reg}_{\alpha\beta}(E_f)\,. \tag{9}$$

Examining the individual terms, we find that the standard transition probability can be obtained by utilizing elements of the PMNS matrix. For the standard transition, there is no decay and thereby $E = E_i = E_f$

$$P^{\rm SM}_{\alpha\beta}(E,L) = |U^*_{\alpha1}U_{\beta1} + U^*_{\alpha2}U_{\beta2}e^{-i\frac{\Delta m^2_{21}}{2E}L} + U^*_{\alpha3}U_{\beta3}e^{-i\frac{\Delta m^2_{31}}{2E}L}|^2. \tag{10}$$

As the high-energy neutrinos oscillate rapidly, the probabilities can be averaged out such that the standard transition is taken to be Eq. 4.
To account for the effects of the decay the following substitution can be made: $\frac{\Delta m^2_{il}}{2E} \to \frac{\Delta m^2_{il}}{2E} - i\frac{\Gamma_i}{2}$, where Γ_i is the decay width of the eigenstate ν_i. This formalism is conventional when dealing with decay, and it is a solution to the Schrödinger equation [15]. The substitution is made into Eq. (10), which will account for both the standard transition probability and the depletion component [1], i.e.,

$$P^{\rm inv}_{\alpha_\beta}(E,L) = |U^*_{\alpha1}U_{\beta1} + U^*_{\alpha2}U_{\beta2}\cdot e^{-i\frac{\Delta m^2_{21}}{2E}L}\cdot e^{-\frac{\Gamma_2}{2}L} + U^*_{\alpha3}U_{\beta3}\cdot e^{-i\frac{\Delta m^2_{31}}{2E}L}|^2\cdot e^{-\frac{\Gamma_3}{2}L}\,, \tag{11}$$

where inv denotes invisible decay.
With calculations found in Appendix A1, the oscillation is averaged out, and the solution for the depletion is found as

$$\bar{P}^{\rm dep}_{\alpha_\beta}(E,L) = -|U_{\alpha2}|^2|U_{\beta2}|^2(1-e^{-\Gamma_2 L}) - |U_{\alpha3}|^2|U_{\beta3}|^2(1-e^{-\Gamma_3 L})\,. \tag{12}$$

The total transition probability for invisible decay is then found as $\bar{P}^{\rm inv}_{\alpha_\beta}(E,L) = \bar{P}^{\rm SM}_{\alpha_\beta} + \bar{P}^{\rm dep}_{\alpha_\beta}(E,L)$. This term does not consider the effects of intermediate decay, so the last part of Eq. (9) that needs consideration is the regeneration component. This expression is significantly more complex than the two previous due to the distinction between the initial and final energies.
If we assume that the decay occurs at a distance L_1 from the source, the regeneration can then be broken down into different sections. Figure 3 shows a schematic drawing for the following process.

- The survival probability of ν_i up to the distance L_1 is characterized by the decay width $e^{-\frac{\Gamma_i}{2}L_1}$.

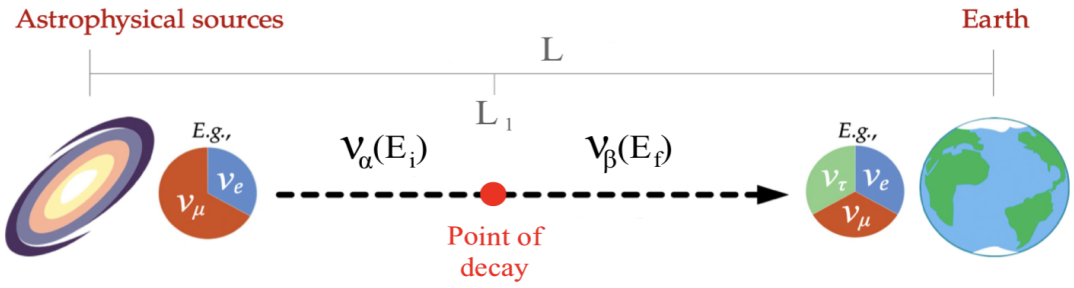

Figure 3. Schematic illustration of the decay.

Due to the effects of oscillation ν_1 accumulates a phase, described by the initial energy $e^{-iE_iL_1}$.

- The decay occurs, resulting in the vanishing of ν_i following an appearance of ν_j. This calculation is in appendix A2.
- The final mass state ν_j survives until the Earth and now has the new decay width $e^{-\frac{\Gamma_j}{2}(L-L_1)}$. This state also accumulates a phase, which is now a function of the final energy $e^{-iE_f(L-L_1)}$.

The total transition probability involves an integral over the decay location L_1 and the initial neutrino energy E_i, which generically can be written as [1]

$$\bar{P}^{\rm reg}_{ij}(E_f, L) = \frac{1}{\Phi^S_i(E_f)} \int_0^L dL_1 \times \int_{E_f}^{x^2_{ij}E_f} dE_i \Delta\bar{P}^{\rm reg}_{ij}(E_i, E_f, L, L_1)\Phi^S_i(E_f) \tag{13}$$

Up until this point, only single decays have been considered, but for $g^{(\prime)}_{21} \neq 0$ and $g^{(\prime)}_{32} \neq 0$, the neutrinos undergo intermediate decays. These can be consecutive: $\nu_3 \to \nu_2 \to \nu_1$ where the states propagate and decay at $L_1 \leq L_2 \leq L$. The process is identical to the earlier one but with more complex integrations. The solution can be separated, such that the full solution for the regeneration for the $\nu_3 \to \nu_1$ transition probability now reads

$$\bar{P}^{\rm reg}_{31} \longrightarrow \bar{P}^{\rm reg}_{31} + \bar{P}^{\rm reg,\ 2}_{31}\,, \tag{14}$$

where the last probability accounts for the consecutive decays. A complete solution for the regeneration can be found in Appendix B2.

3.2 Cosmology Corrections

Astrophysical neutrinos propagate cosmological distances before reaching Earth; thus, they are exposed to the consequences of the expanding Universe.

The redshift of neutrinos depends on a cosmological distance measure, for which there are several different types [19]. Since neutrinos are ultra-relativistic, the relevant distance measurement is the light-travel distance, whereby the time before the decay is directly related to the distance a neutrino has traveled since its production [13]. The light-travel distance used is defined as [1]

$$L(z) = L_H \int_0^z \frac{dz'}{(1+z')^2 h(z')}\,, \tag{15}$$

where $L_H = c/H_0 \simeq 3.89$ Gpc is the Hubble length and $h(z) = H(z)/H_0$ is the normalised Hubble parameter. For a flat ΛCDM cosmology, the definition of $H(z)$ is [19]

$$H(z) \equiv H_0 \sqrt{\Omega_m (1+z)^3 + \Omega}\,, \tag{16}$$

where $\Omega_m = 0.315$ and $\Omega_\Lambda = 1 - \Omega_m = 0.685$. Ω is the density parameter defined as the density ρ divided by the critical density ρ_c, and it determines the overall geometry of the universe [19].

An essential aspect of dealing with the expansion is to correct the neutrino energies, which are now functions of redshift. This correction leads to the following substitution for the energy: $E \to E(1+z)$, which in turn implies: $\Gamma_i \to \Gamma_i/(1+z)$ and $\Gamma_{ij} W_{ij} \to \Gamma_{ij} W_{ij}/(1+z)^2$. The spectra at the source and the point of the decay are no longer the same and also need to be modified, $\Phi_i^S(E_i) \to \Phi_i^S(E_i(1+z)) = \Phi_i^S(E_i)(1+z)^{-\gamma}$ [1].
The final consideration to make is the distribution of sources. The neutrino flux detected by IceCube is approximately diffuse, meaning the neutrino sources have not been definitively located. Thereby we integrate the transition probability and the source distribution, $R(z)$, with respect to the redshift [1]:

$$\bar{P}^{\text{vis}}_{\alpha\beta}(E_f) = \frac{\int_0^{z\ \max} dz \bar{P}^{\text{vis}}_{\alpha\beta}(E_f, z) R(z)}{\int_0^{z\ \max} dz R(z)}\,. \tag{17}$$

In this thesis, we designate the redshift distribution as a delta function $R(z) = \delta(z-1)$, placing all sources at the redshift $z = 1$. Following the substitutions and the redshift distribution, we get the following corrections to the standard, depletion, and regeneration terms [1]:

$$\bar{P}^{SM}_{ij}(z) = \delta_{ij}(1+z)^{-\gamma}\,, \tag{18}$$

$$\bar{P}^{\text{dep}}_{ij}(E_f, z) = -\delta_{ij}(1+z)^{-\gamma}\left(1 - e^{-\Gamma_i L(0,z)}\right)\,, \tag{19}$$

$$\bar{P}^{\text{reg}}_{ij}(E_f, z) = \frac{L_H}{\Phi_i^S(E_f)} \int_0^z dz_1 \int_{E_f(1+z_1)}^{x_{ij}^2 E_f(1+z_1)} dE_i \times \frac{\Gamma_{ij} W_{ij} e^{-\Gamma_i L(z_1,z) - \Gamma_j L(0,z_1)}}{(1+z_1)^2 h(z_1)} \Phi_i^S(E_i(1+z))\,, \tag{20}$$

where $x_{ij} \equiv m_i/m_j$.

4 Analysis Methods

In this chapter, we describe how we processed the data computed with the decay framework. Furthermore, we provide the statistical method used to constrain the neutrino lifetime.

4.1 Energy Averaging

To compare the flavor ratios that we compute to the ones observed at IceCube, we integrate over the energy in the range 60Tev - 3Pev, resulting in energy-averaged flavor ratios. Thereby the flavor-ratios are averaged in energy as such:

$$\langle f_{\alpha,\oplus} \rangle_{E_f} = \frac{1}{E_{f,\max} - E_{f,\min}} \int_{E_{f,\min}}^{E_{f,\max}} \langle f_{\alpha,\oplus}(E_f) \rangle \, dE_f \, . \tag{21}$$

The energy-averaged final flavor ratios as a function of couplings can be seen in Figs. 4, 7, and 8.

4.2 Statistical Method

To constrain the values of the couplings g_{ij} and g'_{ij}, we adopt a Bayesian statistical approach. To simplify our analysis, we fix the scalar and pseudo-scalar couplings to be of equal value, i.e., $g_{21} = g'_{21}$, $g_{31} = g'_{31}$, and $g_{32} = g'_{32}$. We compute the posterior probability density on the couplings:

$$\begin{aligned} \mathcal{P}(g_{21}, g_{31}, g_{32}) = \int & d\vartheta \pi(\vartheta) \\ & \times \mathcal{L}(\langle f_\oplus(g_{21}, g_{31}, g_{32}, \vartheta, f_S) \rangle) \\ & \times \pi(g_{21}) \pi(g_{31}) \pi(g_{32}) \, . \end{aligned} \tag{22}$$

In Eq. 22, $\pi(\vartheta)$ is the prior on the mixing parameters; we take it to be a four-dimensional delta function, centered on the best-fit values of the mixing parameters from ν-fit 5. The likelihood function $\mathcal{L}$ represents the estimated sensitivity to flavor-ratio measurements in current and future neutrino telescopes, from Refs. [11][18]. We consider four scenarios for the likelihood: 8 years of IceCube, 15 years of IceCube, 15 years of IceCube + 10 years of the planned upgrade IceCube-Gen2, and the combined sensitivity of all planned telescopes by 2040[1]. For the couplings, we assume uniform priors $\pi(g_{ij})$ in $\log_{10}(g_{ij})$, to avoid introducing unnecessary bias. For the spectral index γ and the mass of ν_1, we also take uniform priors, $\pi(\gamma)$ and $\pi(m_{\nu,1})$.
When constraining a coupling, the 5D posterior probability is integrated with respect to the other

[1] IceCube+IceCube-Gen2+KM3NeT+Baikal-GVD+P-ONE+TAMBO

couplings. Eg. for g_{21}:

$$\begin{aligned}\mathcal{P}(g_{21}) = \int & d\vartheta dg_{31} dg_{32} \mathcal{L}(\vartheta)\pi(\vartheta) \\ & \times \mathcal{L}(\langle f_{\oplus}(g_{21}, g_{31}, g_{32}, g'_{21}, g'_{31}, g'_{32}, \vartheta, f_S)\rangle) \\ & \times \pi(g_{21})\pi(g_{31})\pi(g_{32})\pi(g'_{21})\pi(g'_{31})\pi(g'_{32})\end{aligned} \tag{23}$$

We maximize the posterior and found confidence intervals around the best-fit point using *MultiNest*, an efficient Bayesian inference tool [20].

The likelihood functions are estimates that have been built to be manually centered on the ternary plot. They were constructed assuming that the flavor ratios at the source are $\frac{1}{3}(1:2:0)$ and standard flavor transitions, i.e., no decay.

The Figure 4 illustrates the evolution of the energy-averaged flavor ratios superimposed on the likelihood function associated to 8 years of IceCube.

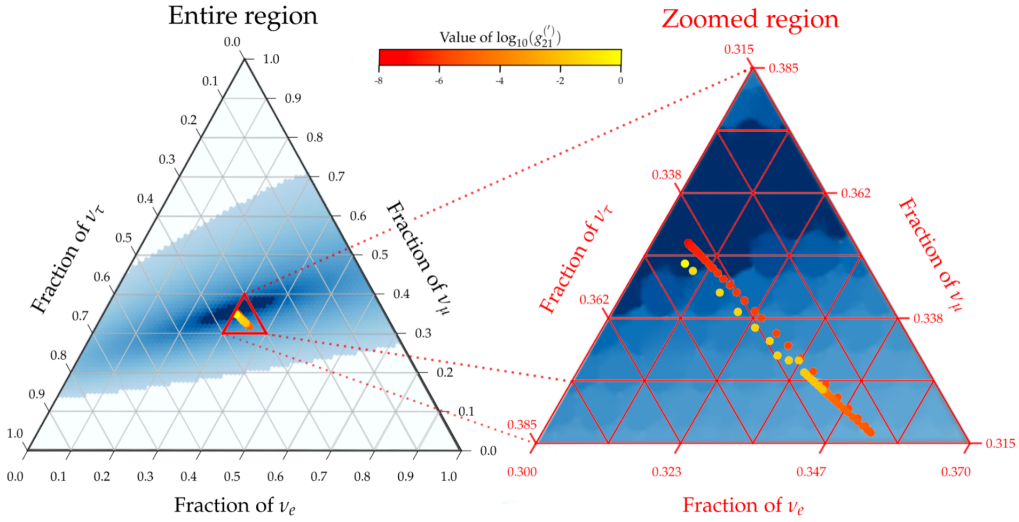

Figure 4. Ternary plot of the energy-averaged flavour ratios as a function of g_{21}. It is displayed on top of the likelihood with 8 years of IceCube. This is the same data that is plotted on the left in Fig. (7). This plot is solely illustrative to emphasize the evolution of the flavor ratios and to show an example of the likelihood functions.

5 Results

The following section is two twofold. First, we use the decay framework to calculate the flavor ratios at Earth and present the impact of varying the decay parameters on the final ratios.

Second, we present the results of the large parameter scan, where we utilize the methods Chapter 4 to

constrain the neutrino lifetime.

When parameters which we vary in the analysis are: $(g_{12}, g_{13}, g_{23}, \gamma, m_1)$, since we set $g_{ij} = g'_{ij}$ in our analysis.. The mixing parameters also influence the visible decay, but these were fixed at their current best fit which are listed in Table 1.

θ_{12}°	θ_{23}°	θ_{13}°	δ_{CP}°
$33.44^{+0.77}_{-0.74}$	$49.0^{+0.9}_{-1.2}$	$8.57^{+0.12}_{-0.12}$	197^{+27}_{-24}

Table 1. Table of the mixing parameters from Nufit 5.0 with the normal mass ordering.

5.1 Varying the Decay Parameters

5.1.1 Spectral index

Fig. 5 shows the flavor ratios at Earth as a function of the spectral index γ.

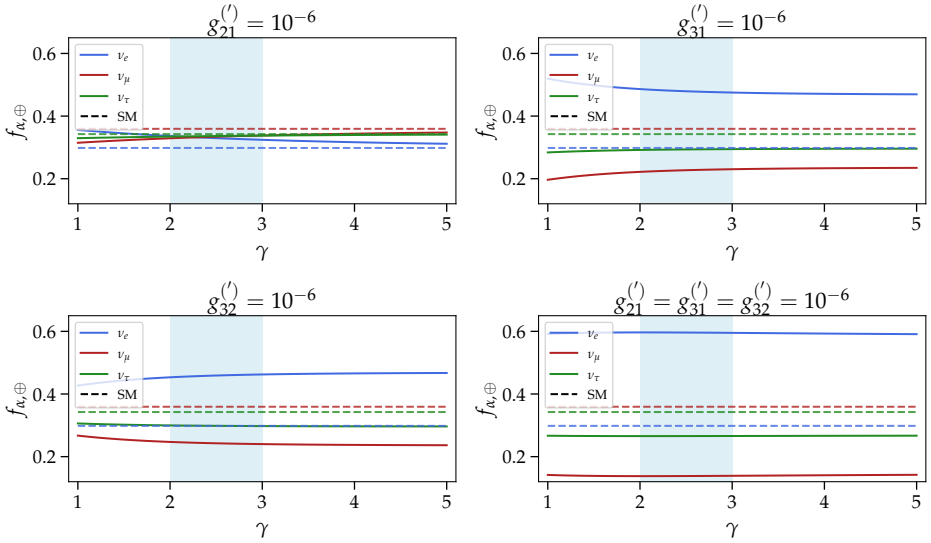

Figure 5. The final flavor ratio as a function of γ from an initial ratio of $\frac{1}{3}(1:2:0)$. The relevant coupling coefficient is shown above the individual plots. For each subplot the rest were turned off, e.g., for the g_{21} plot; $g_{31} = g_{32} = 0$. The mass was set as $m_{\nu_1} = 0.1$eV. The blue shaded region of each subplot indicates the range for which γ was varied when determining the constraints.

The change in the spectral index can have a considerable effect on the final composition. The figure reveals that when the spectral index is small, say $\gamma = 1.5$, the regeneration component from Eq. (3.2)

is significant. Increasing the spectral index results in a decrease of the regeneration, thus the flavor compositions become constant. For $\gamma \longrightarrow \infty$ the invisible decay case is recovered.
To clarify the discrepancy between the different couplings, an analytical solution to the regeneration is found from Ref. [1]. Omitting cosmology and taking the limits of $m_{\nu_1} \to 0$ and $E_f \to 0$ changes the dependency of the spectral index. For the case of only $g_{31}^{(\prime)} \neq 0$, this gives us the analytical solution [1]

$$\bar{P}^{\text{vis}}_{\alpha\beta} = |U_{\alpha 1}|^2|U_{\beta 1}|^2 + |U_{\alpha 2}|^2|U_{\beta 2}|^2 + \frac{|U_{\alpha 3}|^2|U_{\beta 1}|^2}{\gamma}\,. \tag{24}$$

Thus, $f_{\alpha\beta,\oplus} \propto x/\gamma$, where $x = |U_{\alpha 3}|^2|U_{\beta 1}|^2$ in this specific case. For larger values of x, the ratio is less dependant on the spectral index γ. The analytical solutions for $g_{21} \neq 0$ and $g_{31} \neq 0$, along with the computed values for all dependencies are determined in Appendix C. Their behavior parallels that of Fig. 5.

5.1.2 Mass of ν_1

Fig. 6 shows a plot of the final flavor ratio as a function of m_{ν_1}.

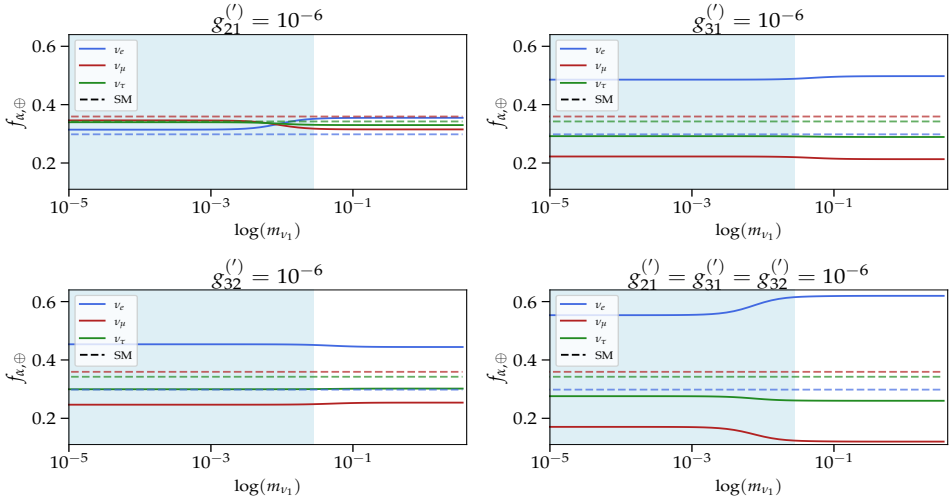

Figure 6. The final flavor ratio as a function of m_{ν_1} from an initial ratio of $\frac{1}{3}(1:2:0)$. The relevant coupling coefficient is shown above the individual plots, and for each subplot, the rest were turned off, e.g., for the g_{21} plot; $g_{31} = g_{32} = 0$. The mass was set as $m_{\nu_1} = 0.1$eV. The blue shaded region of each subplot indicates the range for which m_{ν_1} was varied when determining the constraints.

The mass of ν_2 and ν_3 are set as

$$m_{\nu_2} = \sqrt{\Delta m^2_{21} + m^2_{\nu_1}} \quad \wedge \quad m_{\nu_3} = \sqrt{\Delta m^2_{31} + m^2_{\nu_1}}\,. \tag{25}$$

Varying the mass of the the lightest eigenstate, ν_1, affects the flavor ratios at Earth, since the decay width is proportional to the decay width, which is a function of x_{ij} from Eq.3.2. Since m_{ν_2} and m_{ν_3} are proportional to $\sqrt{m_{\nu_1}}$, the relative distance between the masses decreases as m_{ν_1} increases. Therefore $x_{ij} \longrightarrow 1$ as mnu1 increases
To illustrate this, a closed form solution of the regenerational probability is used. For various values of E_f and m_{ν_1} this gives us the regeneration [1]

$$\bar{P}_{ij}^{\text{reg}} = \frac{z(x)}{2y(x)} \left[\left(1 - \frac{1}{x^4}\right) + \frac{2}{T^2} \left(e^{-T}(1+T) - e^{-T/x^2}(1 + \frac{T}{x^2}) \right) \right] . \tag{26}$$

For $x \longrightarrow 1$ the regeneration will then tend towards zero, recovering the case $E_i = E_f$. Thus only invisible decay has an effect. This depletes the amount of ν_μ and ν_τ and leaves the amount ν_e unchanged, such that the ratio of ν_e increases with respect to the other two. The only exception in Fig. 6 is where only g32 is non-zero; the difference, in this case, is that the regenerated neutrinos are nu_2, not nu_1, which have a lower nu_e content.

5.1.3 Coupling constants

Fig. 7 shows a plot of the energy-averaged flavor ratios at Earth as functions of the coupling constant g_{21}, as well as the ratios as functions of energy for various values of g_{21}.

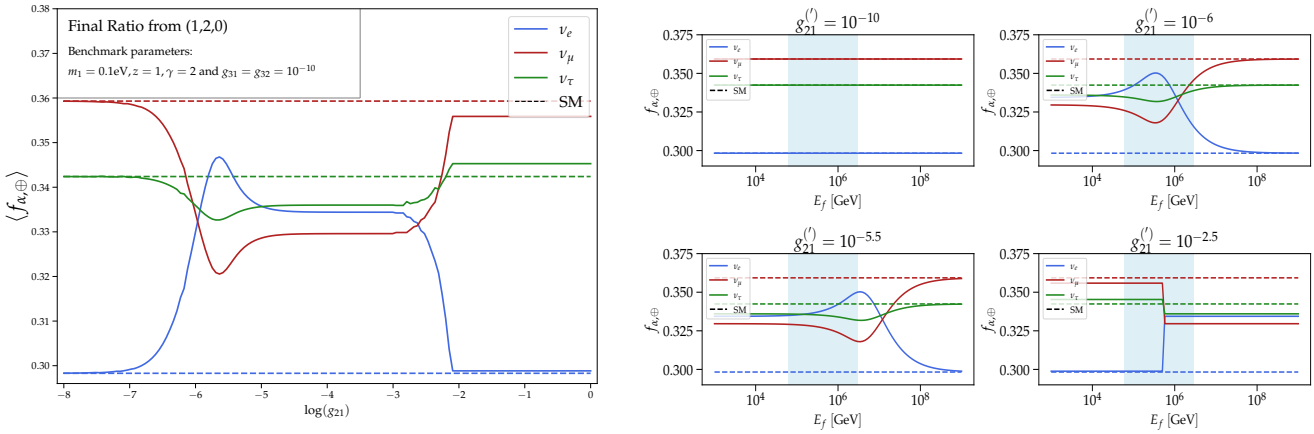

Figure 7. The parameters used in both plots are $\gamma = 2$, m_{ν_1} and $g_{31} = g_{32} = 0$. **Left:** The energy-averaged flavor ratios as a function of the coupling g_{21}. The energy was integrated from $E_{\text{min}} = 40$TeV to $E_{\text{max}} = 6$TeV. **Right:** The flavor ratio as a function of energy for different values of g_{21}.

In Fig. 7 some complex behavior is evident due to the interplay between regeneration and depletion. Therefore we go through each subplot individually and explain the effect on the energy averaged plot:

- In the region $g21 < 10^{-8}$, Fig. 7 shows that, as expected, no decay occurs if the coupling is small.
- In the region $g_{21} \simeq 10^{-6} - 10^{-5.5}$, Fig. 7 shows a noticeable increase fraction of ν_e on the energy averaged plot. Thus, in this coupling region, regeneration has the highest impact on the overall flavor ratio.
  In the two corresponding subplots, the increase in coupling(from $g_{21} = 10^{-6}$ to $g_{21} = 10^{-5.5}$)shows a shift of the regeneration to higher energies, where the regeneration goes to zero. As this transition moves further out of the integrated energy region, it creates the bump in ν_e contents found in the energy-averaged plot. The ratio of ν_μ and ν_τ falls relatively to ν_e.
- In the region $g_{21} > 10^{-2}$, Fig. 7 shows a very apparent phase transition for the ratios as seen on the lower right subplot. This occurs because regeneration tends to a non-zero constant at high values of the coupling. As the coupling increases, this transition shifts to higher energies and thus occurs outside the integrated energy region. This explaining why the ratio returns to values close to the standard transition for the energy-averaged ratios.

As the energy keeps increasing, the regeneration will tend towards zero. As $E \longrightarrow \infty$ the standard case is recovered, and the regeneration goes to zero.
Fig. 8 shows analogous plots of the energy-averaged flavor ratios as a function of g_{31} and g_{32}. These also are driven by the above interplay between depletion and regeneration, though the interplay here is milder, so a more conventional evolution is seen. The flavor ratio never ratios do not return to their standard values at high values of the couplings since the phase transition is not recovered in the appropriate energy interval.

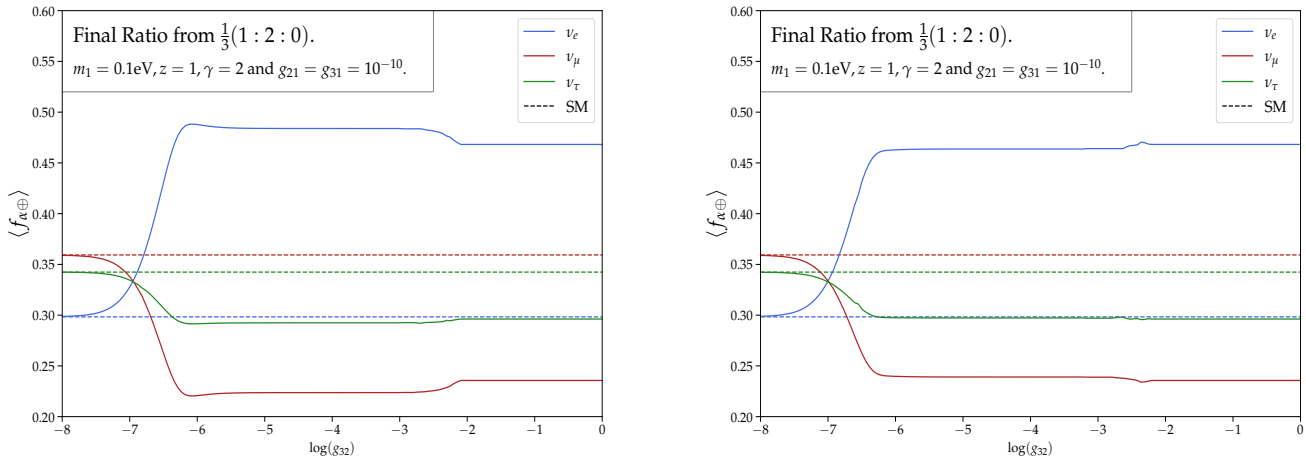

Figure 8. In both plots the energy was integrated from $E_{\min} = 40$TeV to $E_{\max} = 6$TeV. Plots of the flavor-ratio as a function of energy can be found for both in appendix E. **Left:** The energy-averaged flavor-ratios as a function of the coupling g_{31}. **Right:** The energy-averaged flavor-ratios as a function of the coupling g_{32}

5.2 Constraints on the Lifetime

When maximizing the posterior, Eq. (23), the five model parameters $(g_{21}, g_{31}, g_{32}, \gamma, m_{\nu_1})$ are varied simultaneously, and independently of each other. As the goal is to constrain the couplings, m_{ν_1} and γ are nuisance parameters. Furthermore, the mixing parameters were set at their best-fit values.

The spectral index and the mass of the lightest eigenstate are varied in 10 equally spaced linear steps between $2-3$ and $0-0.0281\text{eV}^2$, respectively. The couplings (g_{21}, g_{31}, g_{32}) were varied in 10 equally spaced logarithmic steps between $10^{-8}-10^{0}$. For each of the 10^5 combinations of model parameters, we compute the energy-averaged flavor ratios at Earth, Eq. (21). For in-between values of the model parameters, we interpolate based on our pre-computed grid.

We use MultiNest [20] to maximize the posterior and find credible regions of the model parameters. We did this for each of the four detector likelihood functions; Appendix E shows the correlation between the model parameters in each case. The results are in Table 2, which shows the one-dimensional marginalized allowed ranges for the coupling constants.

In the earlier analysis of the couplings (Figs. 7 & 8) we found that no decay occurred for $g_{21} = g_{31} = g_{32} = 10^{-8}$. Since all of the couplings are consistent with this value, we find that the couplings are compatible with case of no decay. This is because of the nature of the likelihood functions, thus the analysis finds how well the neutrino telescopes can constrain neutrino decay. The results will therefore always be compatible with the case of no decay; the important result is the constraints on the couplings.

	$\log g_{21}^{(\prime)}$		$\log g_{31}^{(\prime)}$		$\log g_{32}^{(\prime)}$	
	Best fit $\pm1\sigma$	$< 2\sigma$	Best fit $\pm1\sigma$	$< 2\sigma$	Best fit $\pm1\sigma$	$< 2\sigma$
IceCube 8yr	$-6.14^{+4.95}_{-1.29}$	< -0.27	$-7.62^{+0.34}_{-0.25}$	< -7.06	$-7.68^{+0.34}_{-0.21}$	< -7.05
IceCube 15yr	$-6.37^{+5.18}_{-1.19}$	< -0.20	$-7.67^{+0.35}_{-0.23}$	< -7.08	$-7.72^{+0.36}_{-0.19}$	< -7.10
IceCube-Gen2	$-7.27^{+3.25}_{-0.48}$	< -0.46	$-7.80^{+0.32}_{-0.15}$	< -7.20	$-7.84^{+0.34}_{-0.12}$	< -7.21
Combined	$-7.41^{+0.53}_{-0.41}$	< -0.56	$-7.89^{+0.19}_{-0.08}$	< -7.36	$-7.90^{+0.13}_{-0.08}$	< -7.47

Table 2. Constraints of the coupling constants. The results were computed with different likelihood functions; the current 8yr likelihood function, as well as the 15yr, the 15yr+Gen2 10yr, and finally a combination of future experiments from various neutrino telescopes. The likelihood functions were obtained from Ref. [11] [18].

The constraints are tighter for g_{31} and g_{32} than for g_{21}. This is because of the behavior determined in Figs. 7 and 8, where the energy-averaged flavor ratios returned to being close to their standard values for high values of g_{21}, but not for high values of g_{31} or g_{32}. In all cases, the no decay region was preferred, and high values for g_{21} exhibited behavior similar to the case of no decay. Furthermore, the

[2] This is the highest allowed value found by combining the upper limit on the sum of neutrino masses, $\sum_i m_{\nu,i} < 0.115$ [21] and the best-fit values of Δm^2_{21} and Δm^2_{31} from Nufit 5.0.

constraints on g_{31} and g_{32} are similar, because of the small difference in the mass between ν_1 and ν_2. Since the mass of the eigenstates are still unknown, we do not provide a specific constraint on the lifetimes, but rather plots of the couplings and lifetimes as a function of m_{ν_1}. Fig. 9 shows the upper bounds on the couplings as functions of m_{ν_1}.

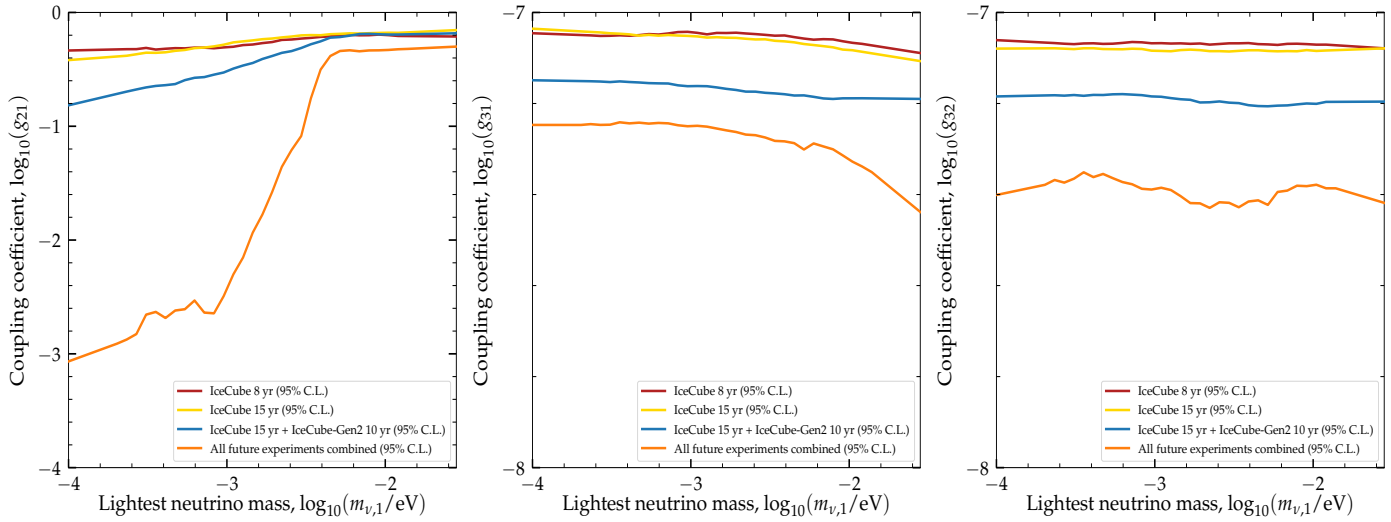

Figure 9. The coupling coefficients, from left to right; g_{21}, g_{31}, and g_{32}, as a function of m_{ν_1}, for the four different likelihood functions used to constrain the couplings.

Fig. 10 shows a plot of the lifetimes as a function of m_{ν_1}. To convert the lower limits from Fig. 9 into the lifetimes of ν_2 and ν_3, we compute the partial decay rate Γ_{ij} via Eq. (28) in Appendix A. We transform the decay rate to the rest frame of the parent neutrino by multiplying Eq. (28) by the boost factor E_i/m_i. For ν_2, the total decay rate is $\Gamma_2 = \Gamma_{21}$, and the lifetime is $\tau_2 = 1/\Gamma_2$. For ν_3, the total decay rate is $\Gamma_3 = \Gamma_{31} + \Gamma_{32}$, and the lifetime is $\tau_3 = 1/\Gamma_3$.

In Fig. 10 it is evident that the constraints on the ν_3 lifetime are considerably higher than for ν_2. In Fig. 1 from [22] we find that the existing constraints on the lifetimes, along with the values provided in Appendix F. The lower limit on τ_3 that we have determined is considerably better than previous ones (from Ref. [23]), while the lower limit on τ_2 is weaker by several magnitudes.

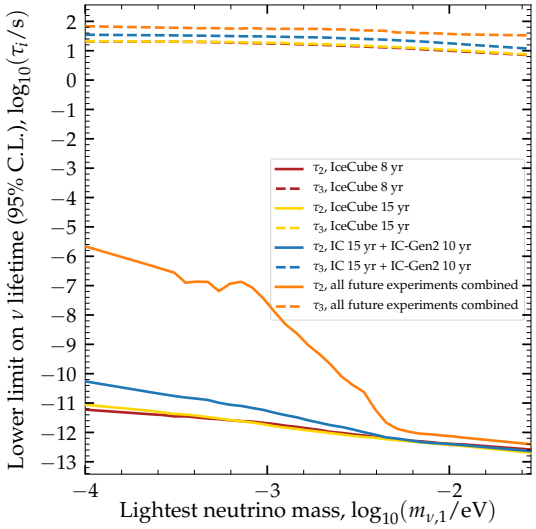

Figure 10. Lower limits of the lifetime of ν_2 and ν_3.

The reason is that in our analysis we allow decay though all channels, such that both ν_2 and ν_3 can decay. Had we focused our analysis on a specific eigenstate, we would have been able to provide tighter constraints, e.g., if we only allowed ν_2 to decay. In our parameter scan we varied all the couplings, but had we fixed some of these, the restraint from the likelihood function would only apply to one decay channel, and thus be able to put a more stringent constraint of the lifetime of this eigenstate.

6 Discussion

In this section, we assess the assumptions made when computing the results and discuss the reason and legitimacy for these. Furthermore, we discuss the general trends of the results.

Analyzing the effects of visible decay is a complex issue since it depends on various components. We analyzed several of these, including the couplings, the neutrino energy, the spectral index, and the mass of ν_1. However, several aspects of the visible decay were not examined, namely; (I) the uncertainty of the mixing parameters, (II) the absolute neutrino mass ordering, (III) the initial neutrino spectrum, (IV) the source distribution, and (V) the nature of neutrinos. We made valid assumptions regarding these factors, but in a complete analysis, these should be considered.

(I) Every mixing parameter was fixed at their current best-fit value. The rationale behind this was because we use projections for the future flavor sensitivity of neutrino telescopes in the analysis, at a time when the mixing parameters will be measured more precisely. The effect of θ_{12} and θ_{23} on the flavor ratios are more significant than the effects of θ_{13} and δ_{CP}, so the first two could have been varied along with the decay parameters.

(II) An extensive understanding of flavor physics requires an understanding of the ordering of neutrino masses. This critical point is currently unknown, with the two possibilities; normal mass ordering ($m_1 < m_2 < m_3$) or inverted mass ordering ($m_1 > m_2 > m_3$). Presently the normal mass ordering is preferred at $< 3\sigma$ [24], which is not conclusive.

(III) High-energy astrophysical neutrinos can be created through several processes, but we only considered considered the canonical case of neutrino production via pion decay, $\frac{1}{3}(1:2:0)$. Other options include neutron-decay sources, $(1:0:0)$, and muon-damped sources, $(0:1:0)$. The creation of ν_τ at the sources is improbable due to the extremely high energies required. Changing the initial flavor ratios would impact the final ratios, as the evolution is from a different state.

(IV) Regarding the neutrino source distribution, we assumed that all the sources were located at the redshift of $z = 1$, to speed up the calculations.. A more correct approach would be to use an source probability distribution - such as the *Yuksel Kistler Beacom Hopkins* (YKBH) distribution [25]. The effects of the YKBH distribution were investigated in Ref. [1], and found only a marginal discrepancy between the results obtained with the two. Appendix G contains a plot of the regeneration transition probability for both.

(V) We did not separately investigate the effects of the scalar interactions vs. pseudo-scalar interactions. However, Ref. [1] found a minimal discrepancy between the two channels.
Some general trends for all plots can be noted. In the standard case (i.e., no decay), the ν_μ fraction is the largest one. Under visible decay, this fraction becomes the smallest one in all cases. In Fig. 4 from Ref. [1] (Appendix H), they found that the ν_μ survival probability was extremely low in the energy region we considered. Thereby the ν_μ flavor state quickly depletes. Furthermore, the survival probability for ν_e is not affected much when introducing decay, explaining why this flavor state dominates.

7 Conclusion

With the decay framework from Ref. [1], we computed a considerable data set of theoretical flavor compositions at Earth, for many different combinations of the model parameters. We studied the effect on the flavor composition of varying individual parameters, in order to gain a deeper understanding of neutrino decay. Adopting a Bayesian statistical approach, and based on the estimated flavor sensitivity of current and upcoming neutrino telescopes, we forecast the constraints of neutrino decay that they will be able to place by measuring the flavor composition of high-energy astrophysical neutrinos.
We conclude the lower limit on τ_3 that we have determined is considerably better than previous ones, while the lower limit on τ_2 is significantly weaker. Furthermore, we find a trend of tighter results with bigger and better neutrino telescopes.
We found the upper 2σ limit as: $\log g_{21}^{(\prime)} < -0.27$, $\log g_{31}^{(\prime)} < -7.06$, and $\log g_{32}^{(\prime)} < -7.05$.

References

1. A. Abdullahi, P. B. Denton, *Physical Review D* **102** (2020) (cit. on pp. II, 1, 6–9, 13–14, 18–19, 21–22, 27).
2. B. Povh, K. Rith, C. Scholz, F. Zetsche, W. Rodejohann, *Particles and Nuclei* (Springer Berlin Heidelberg, 2015) (cit. on pp. 1–2).
3. Z. Chacko, A. Dev, P. Du, V. Poulin, Y. Tsai, *Physical Review D* **103** (2021) (cit. on pp. 1, 6).
4. P. B. Pal, L. Wolfenstein, *Phys. Rev. D* **25**, 766 (1982) (cit. on p. 1).
5. J. F. Nieves, *Phys. Rev. D* **28**, 1664 (1983) (cit. on p. 1).
6. Y. Hosotani, *Nucl. Phys. B* **191**, [Erratum: Nucl.Phys.B 197, 546 (1982)], 411 (1981) (cit. on p. 1).
7. R. Abbasi *et al.*, *Measurement of Astrophysical Tau Neutrinos in IceCube's High-Energy Starting Events*, 2020, arXiv: `2011.03561 [hep-ex]` (cit. on pp. 1, 5).

8. M. Aartsen *et al.*, *Physical Review Letters* **114** (2015) (cit. on p. 1).
9. M. G. Aartsen *et al.*, *The Astrophysical Journal* **809**, 98 (2015) (cit. on p. 1).
10. M. Aartsen *et al.*, *Physical Review D* **99** (2019) (cit. on p. 1).
11. M. G. Aartsen *et al.*, *Journal of Physics G: Nuclear and Particle Physics* **48**, 060501 (2021) (cit. on pp. 1, 5, 10, 16).
12. B. Kayser, *Neutrino Oscillation Physics*, 2013, arXiv: `1206.4325 [hep-ph]` (cit. on pp. 2–4).
13. P. Baerwald, M. Bustamante, W. Winter, *Journal of Cosmology and Astroparticle Physics* **2012**, 020–020 (2012) (cit. on pp. 2, 6, 9).
14. J. W. F. Valle, *Journal of Physics: Conference Series* **53**, 473–505 (2006) (cit. on p. 2).
15. C. Giunti, C. W. Kim, *Fundamentals of Neutrino Physics and Astrophysics* (cit. on pp. 3–4, 7).
16. M. G. Aartsen *et al.*, *Phys. Rev. Lett.* **113**, 101101 (10 2014) (cit. on p. 3).
17. M. Aartsen *et al.*, *Journal of Instrumentation* **12**, P03012–P03012 (2017) (cit. on p. 4).
18. N. Song, S. W. Li, C. A. Argüelles, M. Bustamante, A. C. Vincent, *Journal of Cosmology and Astroparticle Physics* **2021**, 054 (2021) (cit. on pp. 5, 10, 16).
19. B. Ryden, *Introduction to Cosmology* (cit. on p. 9).
20. F. Feroz, M. P. Hobson, M. Bridges, *Monthly Notices of the Royal Astronomical Society* **398**, 1601–1614 (2009) (cit. on pp. 11, 16).
21. P. A. Zyla *et al.*, *PTEP* **2020**, 083C01 (2020) (cit. on p. 16).
22. M. Bustamante, J. F. Beacom, K. Murase, *Physical Review D* **95** (2017) (cit. on p. 17).
23. M. Gonzalez-Garcia, M. Maltoni, *Physics Letters B* **663**, 405–409 (2008) (cit. on p. 17).
24. P. F. de Salas *et al.*, *Journal of High Energy Physics* **2021** (2021) (cit. on p. 18).
25. H. Yüksel, M. D. Kistler, J. F. Beacom, A. M. Hopkins, *The Astrophysical Journal* **683**, L5–L8 (2008) (cit. on p. 18).

Appendices

Appendix A - Decay width:

The lifetime of a neutrino mass eigenstate ν_i in its restframe, can be found as a function of the decay width:

$$\tau_i = \frac{m_i}{E_i \Gamma_i} \quad \text{or} \quad \kappa_i = \frac{1}{E_i \Gamma_i} \tag{27}$$

Where Γ_i is defined as the decay width of for the mass eigenstate.

A1, Depletion:

Using calculations from quantum field theory (QFT) the following can be shown for a partial decay from ν_i to ν_j [1]

$$\Gamma_{ij} = \frac{m_i m_j}{16\pi E_i} \left(g_{ij}^2 \left[f(x_{ij}) + k(x_{ij}) \right] + g_{ij}'^2 \left[h(x_{ij}) + k(x_{ij}) \right] \right) \tag{28}$$

where E_i is the initial energy, $x_{ij} \equiv m_i/m_j$. Both decay channels $\nu_i \to \nu_j$ and $\nu_i \to \overline{\nu_j}$ have been included. The functions from above are

$$\begin{aligned} f(x) &= \frac{x}{2} + 2 + \frac{2}{x}\log(x) - \frac{2}{x^2} - \frac{1}{2x^3}\,, \\ h(x) &= \frac{x}{2} - 2 + \frac{2}{x}\log(x) + \frac{2}{x^2} - \frac{1}{2x^3}\,, \\ k(x) &= \frac{x}{2} - \frac{2}{x}\log(x) - \frac{1}{2x^3}\,. \end{aligned} \tag{29}$$

Eq. 28 and 29 can be found in Ref. [1] as Eq. (6), (7), (8), and (9).

A2, Regeneration:

As the decay products is now visible, there are two energies invovled - the inital E_i and final E_f. The energy then needs to be normalized, which is done with the following distribution:

$$W_{ij} = \frac{1}{\Gamma_i} \frac{d\Gamma(E_i, E_f)}{dE_f} \tag{30}$$

The decay for the different channels is then found through QFT again [1]

$$\begin{aligned}
\Gamma_{ij}^{\nu\nu} W_{ij}^{\nu\nu} &= \frac{m_i m_j}{16\pi E_i^2} \left(g_{ij}^2 \left[A_{ij} + 2 \right] + g_{ij}'^2 \left[A_{ij} - 2 \right] \right) , \\
\Gamma_{ij}^{\nu\bar{\nu}} W_{ij}^{\nu\bar{\nu}} &= \frac{m_i m_j}{16\pi E_i^2} (g_{ij}^2 + g_{ij}'^2) \left(\frac{1}{x_{ij}} + x_{ij} - A_{ij} \right) , \\
\Gamma_{ij}^{\nu\nu,\nu\bar{\nu}} W_{ij}^{\nu\nu,\nu\bar{\nu}} &= \frac{m_i m_j}{16\pi E_i^2} \left(g_{ij}^2 \left[\frac{1}{x_{ij}} + x_{ij} + 2 \right] + g_{ij}'^2 \left[\frac{1}{x_{ij}} + x_{ij} - 2 \right] \right) .
\end{aligned} \tag{31}$$

Here A_{ij} is the regeneration amplitude, defined as

$$A_{ij} = \frac{1}{x_{ij}} \frac{E_i}{E_f} + x_{ij} \frac{E_f}{E_i} . \tag{32}$$

These equations (30 , 31 , 32) can be found in Ref. [1] as equations (16), (17), (18), and (19).

Appendix B - Regeneration integral:

To compute the integral in Eq.(13) we can compute the amplitude function found above in Eq. (32). The amplitude of the regeneration is [1]

$$A_{ij}^{\text{reg, 2}} = e^{-\frac{\Gamma_i}{2} L_1} e^{-\frac{\Gamma_j}{2} (L - L_1)} \sqrt{T_{ij} W_{ij}} . \tag{33}$$

With the change in transitional probability, before and after decay, of regeneration is the amplitude squared:

$$\Delta \bar{P}_{ij}^{\text{reg}}(E_i, E_f, L, L_1) = |A_{ij}^{reg}|^2 . \tag{34}$$

Relative to the scales of the total propagation, the neutrinos promptly loose coherency, thereby the interference can be omitted. The oscillations are averaged out, and the integral over L_1 can be preformed analytically [1]:

$$\int_0^L dL_1 \Delta \bar{P}_{ij}^{\text{reg}}(E_i, E_f, L, L_1) = \frac{\Gamma_{ij} W_{ij}}{\Gamma_i - \Gamma_j} [1 - e^{-(\Gamma_i - \Gamma_j) L}] . \tag{35}$$

For $g_{21}^{(\prime)} \neq 0$ and $g_{32}^{(\prime)} \neq 0$ the neutrinos can experience intermediate decays can happen. These can be consecutive as well; $\nu_3 \to \nu_2 \to \nu_1$ propagating at decaying at $L_1 \leq L_2 \leq L$. The process is identical as before, but now with a new amplitude:

$$A_{31}^{\text{reg, 2}} = e^{-\frac{\Gamma_3}{2} L_1 \sqrt{T_{32} W_{32}}} e^{-\frac{\Gamma_2}{2} (L_2 - L_1)} \sqrt{T_{21} W_{21}} . \tag{36}$$

The total probabillity is then found as

$$\bar{P}_{32}^{\mathrm{reg},2} = \frac{1}{\Phi_i^S(E_f)} \times \int_0^L dL_1 \int_{L_1}^L dL_2 \int_{E_f}^{x_{32}^2 E_f} dE_{\mathrm{int}} \int_{E_{\mathrm{int}}}^{x_{21}^2 E_{\mathrm{int}}} dE_i \times \Delta\bar{P}_{32}^{\mathrm{reg},2}(E_i, E_{\mathrm{int}}, E_f, L, L_1, L_2)\Phi_i^S(E_i) \tag{37}$$

which is preformed analytically,

$$\begin{aligned} &\int_0^L dL_1 \int_{L_1}^L dL_2 \Delta\bar{P}_{32}^{\mathrm{reg},2}(E_i, E_{\mathrm{int}}, E_f, L, L_1, \\ &= \frac{\Gamma_{32} W_{32} \Gamma_{21} W_{21}}{\Gamma_3 - \Gamma_2} \left[\frac{1}{\Gamma_2}(1 - e^{-\Gamma_2 L}) - \frac{1}{\Gamma_3}(1 - e^{-\Gamma_3 L}) \right] . \end{aligned} \tag{38}$$

These can be combined to give the total transition probability from Eq. (14).

Appendix C - Solutions for Eq. (24):

There are nine differet solutions for eq. (24); 3 different solutions for each of the flavors, with each of the couplings turned on.

Since there is still some enate uncertainty to the mixing parameters, the following solutions are just estimates. There are given without uncertainty, and the values are chosen as the current best fit from the PMNS-matrix. This is not a problem since only the approximate values are needed, in order to explain the development. For larger inverse dependence on the spectral index, the less change is expected as γ increases.

$\mathbf{g_{21}^{(\prime)} \neq 0}$: $\quad \bar{P}_{\alpha\beta}^{\mathrm{vis}} \propto \dfrac{|U_{\alpha 2}|^2 |U_{\beta 1}|^2}{\gamma} \quad \Rightarrow \quad \bar{P}_{\alpha\beta}^{\mathrm{vis}} \propto \dfrac{5}{\gamma \cdot 10^2} .$

$\mathbf{g_{31}^{(\prime)} \neq 0}$: $\quad \bar{P}_{\alpha\beta}^{\mathrm{vis}} \propto \dfrac{|U_{\alpha 3}|^2 |U_{\beta 1}|^2}{\gamma} \quad \Rightarrow \quad \bar{P}_{\alpha\beta}^{\mathrm{vis}} \propto \dfrac{4}{\gamma \cdot 10^2} .$

$\mathbf{g_{32}^{(\prime)} \neq 0}$: $\quad \bar{P}_{\alpha\beta}^{\mathrm{vis}} \propto \dfrac{|U_{\alpha 3}|^2 |U_{\beta 2}|^2}{\gamma} \quad \Rightarrow \quad \bar{P}_{\alpha\beta}^{\mathrm{vis}} \propto \dfrac{3}{\gamma \cdot 10^2} .$

Appendix D - Flavor vs. energy plots for g_{31} and g_{32}:

For both plots the parameters used were benchmark parameters, Table (1), except for the couplings where the other two were turned of. Notice that the energy-averaged region is shown in blue.

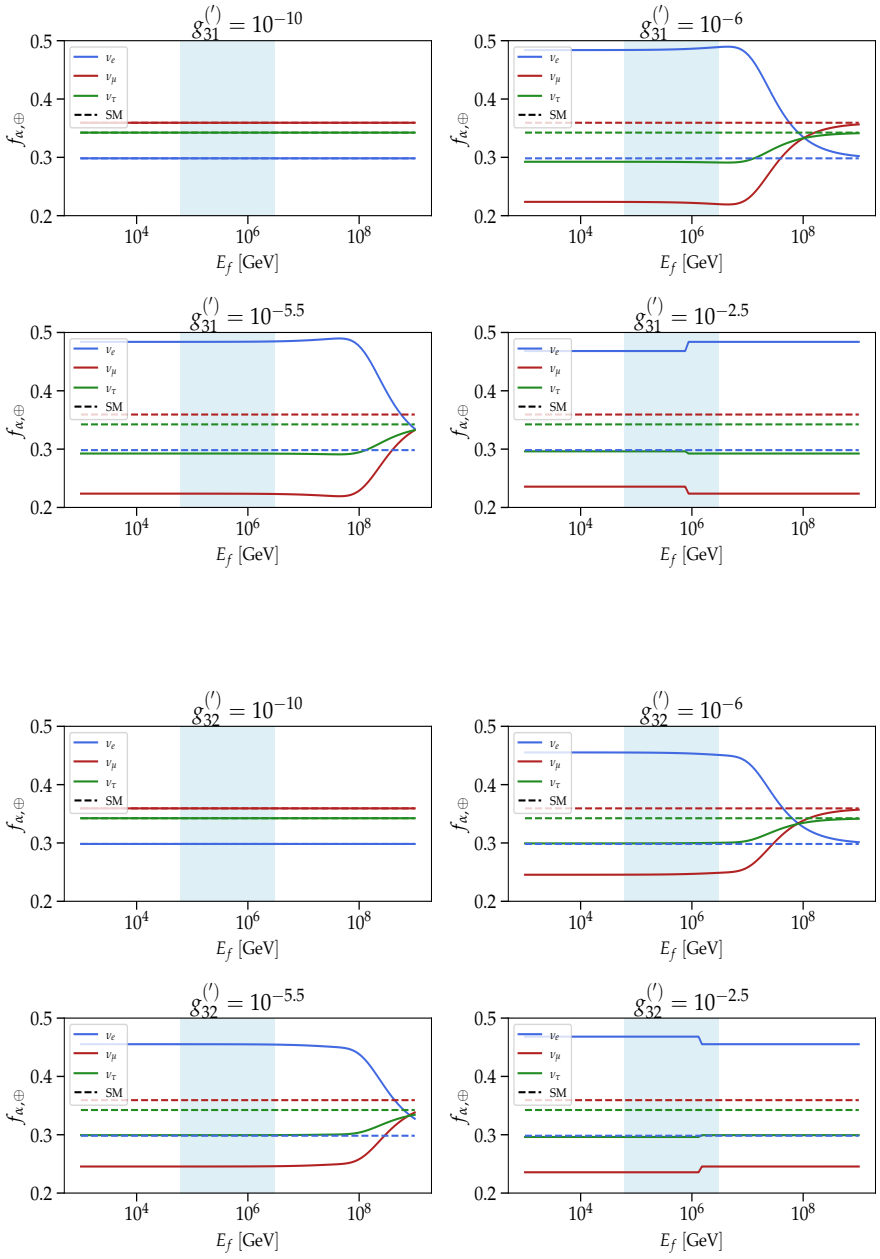

Figure 11. The flavor ratio as a function of energy for different values of **top:** g_{31} and **bottom:** g_{32}.

Appendix E - Posterior probability intersections

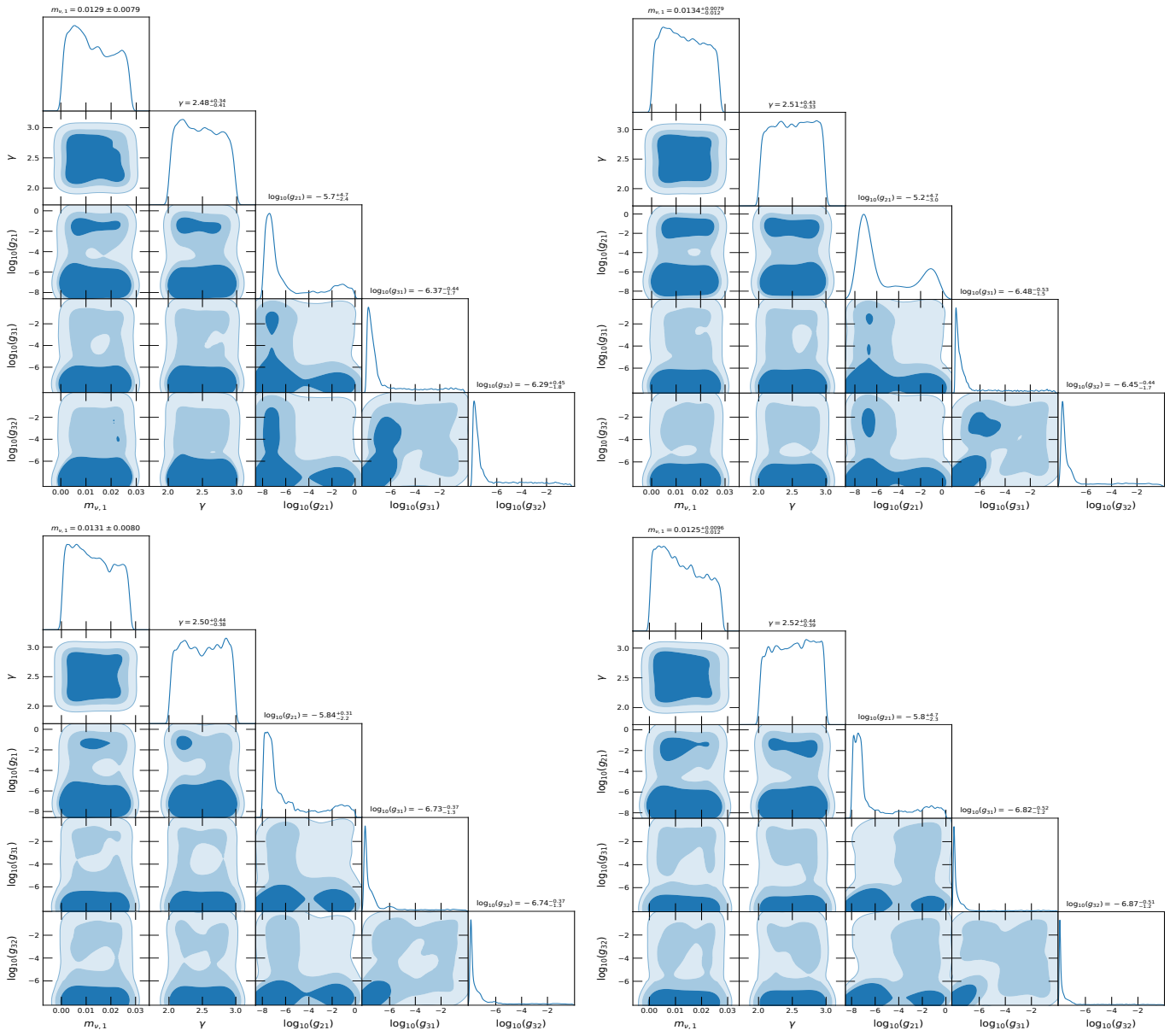

Figure 12. The results of computing the posterior probability for different parameters, as functions of the rest. The dark blue region indicates the 1σ region, the lighter shade indicates 90% confidence, and the lightest shade indicates 97% confidence. The plots are for different likelihood functions.
Upper left: The current likelihood from IceCube after 8 years. **Upper right:** The expected likelihood from IceCube after 15 years. **Lower left:** The expected likelihood from IceCube after 15 years along with running Gen 2 for 10 years. **Lower left:** Combined likelihood from upcoming neutrino experiments from several different telescopes.

Appendix F - Existing Constraints

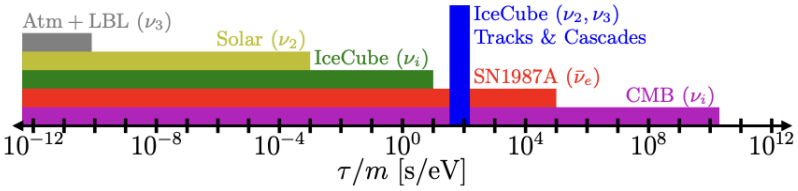

Figure 13. Figure from Ref. [1], with the constraints from Ref. [2-8].

At this point, numerous existing constraints on the lifetime of the neutrinos comes from a wide range of experiments. These can be seen in Fig. 13. Typically the most robust constraints are from the long baseline and low energy neutrinos. The weakest constraints are from atmospheric, accelerator, and reactor neutrinos, which apply primarily to ν_3 decays. Next are the constraints from solar neutrinos, which apply to ν_2 decay. These constraints then apply to all decay channels. Lastly, strong constraints come from the CMB, which affects all of the mass states.
The current constraints, all with a 90% confidence and given as $\kappa_i = \frac{\tau_i}{m_i}$, are [9] [8]

$$\begin{aligned} \kappa_1 &> 2.91 \cdot 10^{-3} \ \frac{\text{s}}{\text{eV}} \ \text{[9]}, \\ \kappa_2 &> 1.26 \cdot 10^{-3} \ \frac{\text{s}}{\text{eV}} \ \text{[9]}, \\ \kappa_3 &> 9.4 \cdot 10^{-11} \ \frac{\text{s}}{\text{eV}} \ \text{[8]}. \end{aligned} \tag{39}$$

References: Constraints

1. A. Abdullahi, P. B. Denton, *Physical Review D* **102** (2020) (cit. on p. 26).
2. B. Aharmim *et al.*, *Physical Review D* **99** (2019) (cit. on p. 26).
3. P. B. Denton, I. Tamborra, *Phys. Rev. Lett.* **121**, 121802 (12 2018) (cit. on p. 26).
4. M. Escudero, M. Fairbairn, *Phys. Rev. D* **100**, 103531 (10 2019) (cit. on p. 26).
5. K. Hirata *et al.*, *Phys. Rev. Lett.* **58**, 1490–1493 (14 1987) (cit. on p. 26).
6. M. Bustamante, J. F. Beacom, K. Murase, *Phys. Rev. D* **95**, 063013 (6 2017) (cit. on p. 26).
7. B. Aharmim *et al.*, *Phys. Rev. D* **99**, 032013 (3 2019) (cit. on p. 26).
8. M. Gonzalez-Garcia, M. Maltoni, *Physics Letters B* **663**, 405–409 (2008) (cit. on p. 26).
9. M. Bustamante, *New limits on neutrino decay from the Glashow resonance of high-energy cosmic neutrinos*, 2020, arXiv: `2004.06844 [astro-ph.HE]` (cit. on p. 26).

Appendix G - Redshift distributions

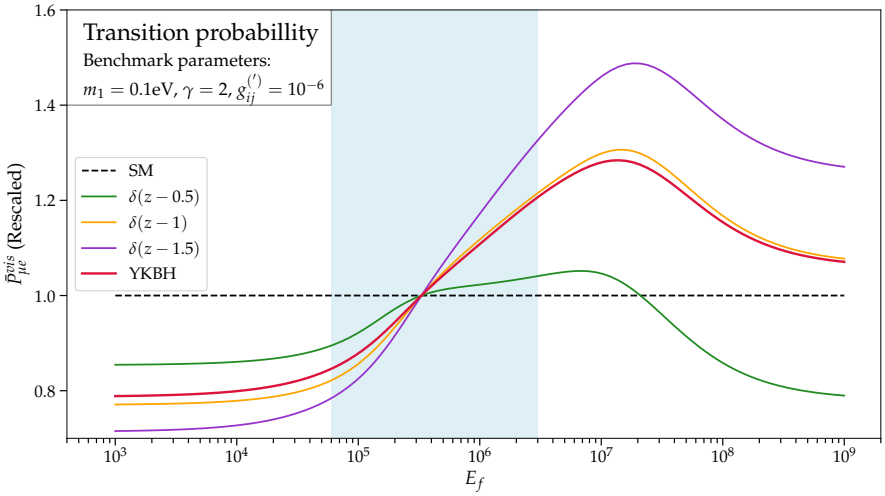

Figure 14. Varying different redshift distributions: $\bar{P}_{\alpha\beta}^{\text{vis}}$ as a function of E_f for the $\nu_\mu \longrightarrow \nu_e$ transition. All curves are normalized to $E_f \simeq 300$ TeV for plotting purposes. This figure is similar to Fig. 3 on the bottom right in Ref. [1].

Appendix H - Figure from Ref. [1]

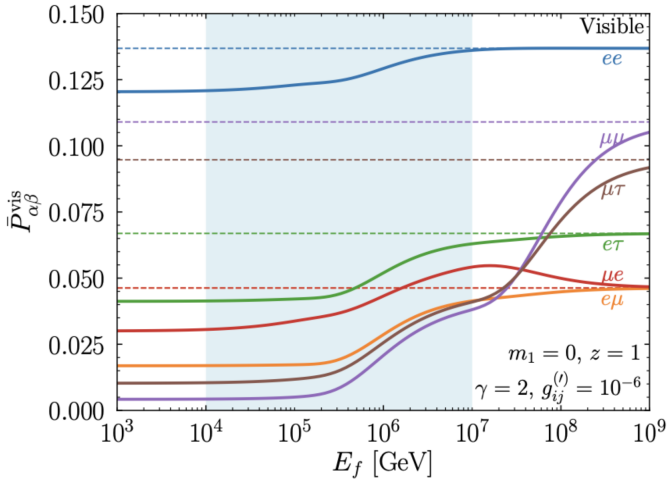

Figure 15. Fig. 4 in Ref. [1]. The visible transition probability as a function of the energy for different transitions.